

The luminous type IIn supernova SN 2017hcc: Infrared bright, X-ray, and radio faint

Poonam Chandra   1,2★ Roger A. Chevalier,³ Nicholas J. H. James³ and Ori D. Fox  

¹National Radio Astronomy Observatory, 520 Edgemont Road, Charlottesville VA 22903, USA

²National Centre for Radio Astrophysics, Tata Institute of Fundamental Research, Ganeshkhind Pune 411007, India

³Department of Astronomy, University of Virginia, P.O. Box 400325, Charlottesville VA 22904-4325, USA

⁴Space Telescope Science Institute, 3700 San Martin Drive, Baltimore MD 21218, USA

Accepted 2022 October 6. Received 2022 September 17; in original form 2022 June 20

Downloaded from <https://academic.oup.com/mnras/article/517/3/4151/6761413> by guest on 26 November 2023

ABSTRACT

We present multiwavelength observations of supernova (SN) 2017hcc with the *Chandra* X-ray telescope and the X-ray telescope onboard *Swift* (*Swift-XRT*) in X-ray bands, with the Spitzer and the TripleSpec spectrometer in near-infrared (IR) and mid-IR bands and with the Karl G. Jansky Very Large Array (VLA) for radio bands. The X-ray observations cover a period of 29 to 1310 d, with the first X-ray detection on day 727 with the *Chandra*. The SN was subsequently detected in the VLA radio bands from day 1000 onwards. While the radio data are sparse, synchrotron-self absorption is clearly ruled out as the radio absorption mechanism. The near- and the mid-IR observations showed that late time IR emission dominates the spectral energy distribution. The early properties of SN 2017hcc are consistent with shock breakout into a dense mass-loss region, with $\dot{M} \sim 0.1 \text{ M}_\odot \text{ yr}^{-1}$ for a decade. At few 100 d, the mass-loss rate declined to $\sim 0.02 \text{ M}_\odot \text{ yr}^{-1}$, as determined from the dominant IR luminosity. In addition, radio data also allowed us to calculate a mass-loss rate at around day 1000, which is two orders of magnitude smaller than the mass-loss rate estimates around the bolometric peak. These values indicate that the SN progenitor underwent an enhanced mass-loss event a decade before the explosion. The high ratio of IR to X-ray luminosity is not expected in simple models and is possible evidence for an asymmetric circumstellar region.

Key words: radiation mechanisms: general – radiation mechanisms: non-thermal – circumstellar matter – supernovae: general – supernovae: individual: (SN 2017hcc).

1 INTRODUCTION

The IIn class of supernovae (SNe IIn) was identified by Schlegel (1990) based on their narrow optical emission lines and hot continua. The narrow lines can be attributed to slow-moving circumstellar (CS) matter around the supernova (SN) and the luminosity can be identified with power provided by shock waves. If the cooling time for the gas is fast compared to the age, the SN power is efficiently converted to radiation in this class of supernovae (SNe). The required density of the circumstellar medium (CSM) is high in several SNe IIn (e.g. Fransson et al. 2014) and are generally not seen in Galactic sources outside of Luminous Blue Variables (LBVs) during outburst (Smith & Owocki 2006; Van Marle, Owocki & Shaviv 2008). Radioactivity is not a suitable power source for these SNe because it predicts a faster decline than observed.

In general, the first electromagnetic signal in SNe occurs when the shock reaches the SN photosphere and breaks out on time-scales of minutes to hours. However, in dense winds shock breakout can happen in the CSM and last for an extended duration. There is increasing evidence that in some SNe IIn, the early light curves can be powered by shock breakouts (Chevalier & Irwin 2011; Ofek et al. 2014; Waxman & Katz 2017).

The early optical spectra of SNe IIn often shows emission lines from a wind that are broadened by electron scattering (Chugai 2001). Photons from the inner part of the mass-loss region scatter as they leave the mass-loss region. An electron column optical depth of about a few, or $10^{24} \text{ electrons cm}^{-2}$ column density, is needed to be consistent with the observations. At later times ($> 100 \text{ d}$), the line profiles are no longer consistent with electron scattering. Profiles are often fit by multiple Gaussians (e.g. Kiewe et al. 2012; Szalai et al. 2021). Although reasonable fits can be obtained, there is not a clear theory that points to Gaussian line shapes. Velocities corresponding to the line widths are larger than the thermal velocities in the optically emitting gas.

Considering the fast shock waves moving into a dense CSM, strong X-ray emission can be expected. Indeed, SNe IIn are well represented among the most X-ray luminous SNe (Dwarkadas & Grusko 2012; Chandra 2018). However, there are optically luminous SNe IIn that are weak X-ray emitters; a prime example is SN 2006gy (Ofek et al. 2007; Smith et al. 2007). In some cases, the paucity of X-rays can be explained by the effects of high X-ray absorption due to the large column density through the CS matter (Chevalier & Irwin 2012; Svirski, Nakar & Sari 2012). Low X-ray luminosity can also be attributed to a relatively low density CSM, as in the case of SN 1998S (Pooley et al. 2002). Chevalier & Irwin (2011) have shown that in some SNe high optical luminosity and low X-ray luminosity can be explained by shock breakout in dense surroundings.

* E-mail: pchandra@nrao.edu

SNe IIn can also be radio emitters from synchrotron radiation by shock accelerated electrons. Many high luminosity SNe IIn are also found to be weak emitters in radio bands (Chandra et al. 2015). While one expects a high intrinsic radio luminosity owing to a dense CSM, the same high density CSM could lead to efficient absorption of radio emission, e.g. the bright Type IIn SN 2010jl became radio bright only after 500 d (Chandra et al. 2015). Thus radio emission in SNe IIn is likely to be an interplay between the two. Internal free–free absorption (FFA) can also play an important role in these SNe due to efficient mixing of cool gas between forward and reverse shock into the synchrotron emitting region (Weiler, Panagia & Sramek 1990; Chandra et al. 2012, 2020).

Gerardy et al. (2002) first described the late bright infrared (IR) emission from SNe IIn in which the IR light dominates the spectral energy distribution (SED). Such emission has been observed in many SNe IIn, including SN 1995N (Van Dyk 2013), SN 1998S (Fassia et al. 2000; Gerardy et al. 2000; Mauerhan & Smith 2012), SN 2006jd (Fox et al. 2011; Stritzinger et al. 2012), SN 2007rt (Trundle et al. 2009; Szalai et al. 2021), SN 2010jl (Fransson et al. 2014; Bevan et al. 2020), SN 2005ip (Fox et al. 2009, 2010; Stritzinger et al. 2012; Bak Nielsen, Hjorth & Gall 2018), SN 2013L (Andrews et al. 2017) etc., beginning at an age of ~ 1 yr. The IR emission in these SNe has an approximately blackbody distribution, with a temperature T in the range ~ 700 –1800 K, which suggests that the emission is from dust.

There are two uncertainties about the dust emission: where is it located and how is it powered. Gerardy et al. (2002) and Fox et al. (2011) argue that the IR emission is from pre-existing dust that is beyond the evaporation radius and the forward shock front. In this case, a decline of the IR emission is expected once the forward shock has overrun the dust shell, around 3–4 yr after the explosion. Such a trend has been seen in some SNe IIn (Fox et al. 2011). On the other hand, efficient dust formation has been considered to be a viable scenario in interacting SNe, as the dust can form rapidly in the extremely dense, post-shock cooling layers (Smith 2014). Gall et al. (2014) and Sarangi, Dwek & Arendt (2018) propose that the dust in SN 2010jl formed in the cold dense shell (CDS) downstream from the radiative shock wave. They find that the dust can form at an age of about 1 yr, when there is an increase in the IR emission from the SN. At earlier times, the radiation field is too strong to allow dust formation. In addition, dust may also form in the inner SN ejecta. Signatures of the dust formation were reported in SN 2006jc (Smith, Foley & Filippenko 2008), SN 2005ip (Smith et al. 2009), and SN 2010bt (Elias-Rosa et al. 2018). The main signatures of dust formation are an IR excess, a drop in optical brightness via dust extinction, and asymmetry of the emission line profiles due to dust attenuation (Smith 2014).

While the most straightforward source for powering the late IR emission in SNe IIn would be continuing CS interaction, for SN 2010jl, the evolution of the X-ray absorption column implies a drop in the CSM density at an age of about 1 yr (Chandra et al. 2015; Sarangi et al. 2018; Dwek et al. 2021). The density drop would result in a drop in the power produced at the forward shock. To alleviate this Sarangi et al. (2018) suggested that the observed power is produced at the reverse shock wave, but the issue is unsettled.

SN 2017hcc (a.k.a ATLAS17lsn) was discovered on 2017 October 2.38 UT (MJD 58028.38) by the Asteroid Terrestrial-impact Last Alert System (ATLAS; Tonry 2011) and classified as Type IIn SN (Prieto et al. 2017). The SN reached a peak at 13.7 mag in around 40–45 d, indicating an absolute peak magnitude of -20.7 mag at a distance ~ 75 Mpc (Prieto et al. 2017). The supernova was not detected on 2017 September 30.4 at a limiting magnitude of

19.04¹ mag, suggesting it was discovered soon after the explosion. We assume 2017 October 1 UT (MJD 58027) as the date of explosion throughout this paper.

Prieto et al. (2017) obtained a bolometric light curve by using a blackbody function to fit the SED using the data from All-Sky Automated Survey for Supernovae (ASAS-SN) Shappee 2014 and the ultraviolet telescope (UVOT) onboard *Swift*. They obtained a peak luminosity of $L_{\text{bol, peak}} = (1.34 \pm 0.14) \times 10^{44}$ erg s $^{-1}$, making SN 2017hcc one of the most luminous SNe IIn ever (e.g. Smith et al. 2007; Ofek et al. 2014). They constrain the peak risetime to be ~ 27 d and the total radiated energy $\sim 4 \times 10^{50}$ erg. Early radio observations at 1.4 GHz with the Giant Metrewave Radio Telescope resulted in a non-detection (Nayana & Chandra 2017).

A very high degree of intrinsic polarization at optical wavelengths was detected from SN 2017hcc (> 4.8 per cent) (Mauerhan et al. 2017; Kumar et al. 2019). This is the strongest continuum polarization ever reported for a SN. Kumar et al. (2019) noted a 3.5 per cent change in the Stokes V polarization in 2 months suggesting a substantial variation in the degree of asymmetry in either the ejecta and/or the surrounding medium of SN 2017hcc. They also estimated a mass-loss rate of $\dot{M} = 0.12 \text{ M}_\odot \text{ yr}^{-1}$ (for a wind speed of 20 km s $^{-1}$), which is comparable to the mass-loss rate for an LBV in eruption. However, based on echelle spectra, Smith & Andrews (2020) suggested the CSM wind to be flowing axi-symmetrically with wind speeds of $v_w = 40$ –50 km s $^{-1}$ indicating bipolar geometry of the CSM created by losing 10 M_\odot of stellar mass to eruptive mass ejections. Smith & Andrews (2020) modelled the optical and near-IR emission of SN 2017hcc and found indications that the SN ejecta were hidden behind the photosphere until day 75. They found that the early time symmetric profiles changed to asymmetric blueshifted profiles at late times. They suggested the asymmetry to be time and wavelength dependent, causing a systematic blueshift in the line profiles. This was interpreted as a signature of the formation of new dust in the SN ejecta as well as in the post-shock gas within the CDS formed between the forward and the reverse shocks.

We carried out early to late time observations of SN 2017hcc with the *Chandra* and the X-ray telescope (XRT) onboard the *Neil Gehrels Swift Observatory* (*Swift*-XRT) telescopes in X-ray bands, with the Karl G. Jansky Very Large Array (VLA) in radio bands, and with *Spitzer* and the TripleSpec in IR bands. In this paper, we report multiwaveband observations of SN 2017hcc and their interpretation. The observations are described in Section 2. Our main results are summarized in Section 3, and the discussion and comparison with published data are in Section 4. Finally, our main conclusions are summarized in Section 5.

2 OBSERVATIONS

2.1 *Chandra* observations

We observed SN 2017hcc with the *Chandra* ACIS-S on 2019 September 27 (MJD 58753) for an exposure of 40 ks. We extracted the spectrum, response and ancillary matrices using CHANDRA INTERACTIVE ANALYSIS OF OBSERVATIONS software (CIAO; Fruscione et al. 2006), using task SPECEXTRACTOR. The CIAO version 4.6 along with CALDB version 4.5.9 was used for this purpose. The HEASOFT² package Xspec version 12.1 (Arnaud 1996) was used to carry out the spectral analysis. Due to low counts, only 5 channels were averaged

¹<https://wis-tns.weizmann.ac.il/object/2017hcc/discovery-cert>

²<http://heasarc.gsfc.nasa.gov/docs/software/lheasoft/>

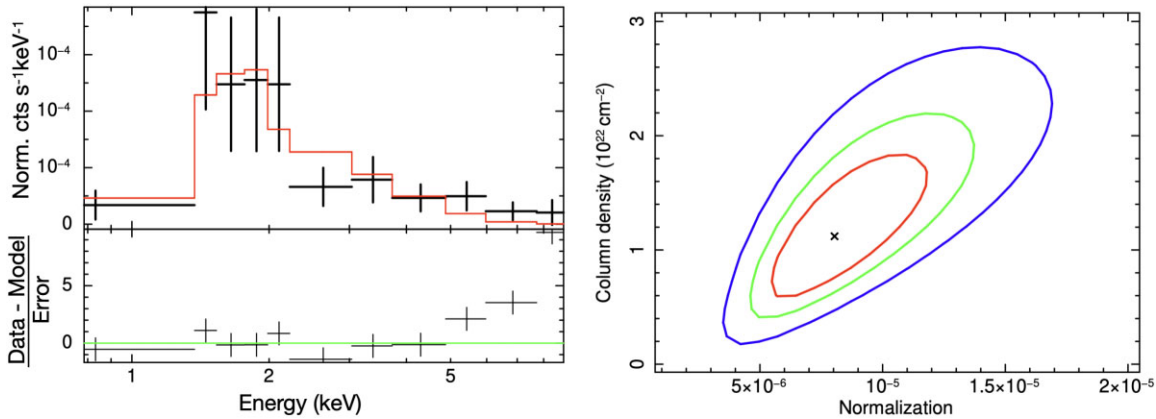


Figure 1. Left-hand panel: *Chandra* ACIS-S spectrum of SN 2017hcc. The spectrum is fit with a thermal bremsstrahlung spectrum assuming a temperature of 3 keV. Right-hand panel: Contours of best fit column density with the best fit normalization. The red, green, and blue lines represent 1 σ , 2 σ , and 3 σ contours.

and we used maximum likelihood statistics for a Poisson distribution, i.e. the *c*-statistics (Cash 1979).

The spectrum was fit with an absorbed thermal bremsstrahlung model. In the view of Smith & Andrews (2020), the optical measurements implied a SN ejecta velocity of 4000 km s⁻¹ around the *Chandra* epoch and a CDS velocity of 1600 km s⁻¹. Assuming the CDS velocity to be that of the forward shock, the reverse shock velocity is 2400 km s⁻¹ (Smith & Andrews 2020). However, in SNe IIn the CDS generally absorbs any X-ray emission coming from the reverse shock due to the high column density of cool gas, and the dominant emission is likely to come from the forward shock (Margutti et al. 2014; Ofek et al. 2014; Chandra et al. 2015). The forward shock velocity of 1600 km s⁻¹ estimated by Smith & Andrews (2020) corresponds to a temperature of \sim 3 keV, which is what we initially assume to fit the *Chandra* spectrum. Our observation resulted in a detection with an unabsorbed 0.3–10 keV luminosity of 1.94×10^{40} erg s⁻¹. The best fit column density is $1.13^{+0.78}_{-0.58} \times 10^{22}$ cm⁻² (Fig. 1).

We, however, note that the forward shock velocity could be larger than the above value, as discussed in Section 4.1. To reflect this possibility, we also ran the fits by fixing the X-ray emitting shocked plasma temperature to be 20 keV [corresponding to a forward shock velocity of 4000 km s⁻¹, an estimate based on observations of SN 2010jl at an age of 737 d (Ofek et al. 2014; Chandra et al. 2015)]. In this case, our observation resulted in an unabsorbed 0.3–10 keV luminosity of 1.74×10^{40} erg s⁻¹. The best fit column density is $(5.7^{+6.2}_{-4.5}) \times 10^{21}$ cm⁻². While the X-ray luminosity is lower by only 10 per cent for 20 keV plasma as compared to that with 3 keV plasma, the best fit column density is lower by a factor of 2, though we note that the uncertainty in column density is large with a 3 σ upper limit of $\sim 2 \times 10^{22}$ cm⁻². Hence this is roughly consistent with the previous value.

2.2 *Swift*-XRT observations

We observed SN 2017hcc with the *Swift*-XRT starting 2017 October 28 (MJD 58054). The observations continued until 2021 May 03 (MJD 59337) at various epochs. The measurements were taken in the photon counting mode. The `xselect` program of the HEASOFT package (version 6.28, CALDB version (XRT(20210915))) was used to create the spectra and images. Observations closely spaced in time were combined. None of the *Swift*-XRT observations resulted in detection with 3 σ upper limits ranging around $\sim(1\text{--}4) \times 10^{-3}$

counts s⁻¹. The 0.3–10.0 keV flux was obtained from the 3 σ upper limits on the count rates by assuming a thermal plasma of 3 keV and a column density of 1.1×10^{22} cm⁻². The details are given in Table 1.

2.3 Spitzer observations

SN 2017hcc was observed with the Infrared Array Camera (IRAC) (Fazio et al. 2004) onboard *Spitzer* (Werner et al. 2004) at three epochs (PI: Fox), starting 2018 October 29 (MJD 58420; Table 2). We used the Spitzer Heritage Archive (SHA)³ to download Post Basic Calibrated Data (pbcd), which are already fully coadded and calibrated. Standard aperture photometry was performed, although separate apertures were strategically placed by eye to best estimate the local background. Fig. 2 plots and Table 2 lists the mid-IR photometric data, which are also included in a comprehensive *Spitzer* paper by Szalai et al. (2021).

As in the analysis laid out by Fox et al. (2011), the mid-IR photometry can be fit as a function of the dust temperature, T_d , and mass, M_d . Given only two photometry points per epoch, we assume a simple blackbody model, consisting of a single graphite grain of size 1 μ m and a single temperature. We calculate opacities using the optical constants from Draine & Lee (1984). Table 2 lists the results and Fig. 2 shows the *Spitzer* data.

2.4 TripleSpec observations

We obtained five epochs, 2017 December 05 (MJD 58092), 2018 January 6 (MJD 58124), September 18 (MJD 58379), November 02 (MJD 58424) and 2019 January 17 (MJD 58500), of near-IR spectroscopy, with simultaneous continuous wavelength coverage from 0.95–2.46 μ m in five spectral orders, with the TripleSpec spectrograph at the Apache Point Observatory 3.5 m (Wilson et al. 2004). Our observation sequence consists of 300 s dithered exposures that could be pair subtracted to allow for correction of thermal background and night-sky emission lines. We used a modified version of SpeXTool for the spectral extraction (Cushing 2004). While the early data are dominated by shorter wavelength emission, the later data reveal higher flux densities at longer wavelengths (Fig. 3). However, we note a caveat here that due to calibration uncertainty the TripleSpec flux should not be considered absolute and ideally should be scaled to near-IR photometry.

³<https://sha.ipac.caltech.edu>

Table 1. X-ray observations of SN 2017hcc.

Date of Observation (UT)	MJD	Telescope	Exposure (ks)	Age (day)	Count rate (cts s ⁻¹)	Unabs. Flux (erg s ⁻¹ cm ⁻²)	Unabs. Luminosity (erg s ⁻¹)
~ 2017 Oct 30	58056	<i>Swift</i> -XRT	13.47	29	<1.02 × 10 ⁻³	<0.54 × 10 ⁻¹³	<3.64 × 10 ⁴⁰
~ 2017 Nov 17	58074	<i>Swift</i> -XRT	5.20	47	<2.56 × 10 ⁻³	<1.35 × 10 ⁻¹³	<8.97 × 10 ⁴⁰
~ 2017 Dec 10	58097	<i>Swift</i> -XRT	9.58	70	<1.03 × 10 ⁻³	<0.55 × 10 ⁻¹³	<3.65 × 10 ⁴⁰
2018 May 23	58261	<i>Swift</i> -XRT	4.94	235	<3.85 × 10 ⁻³	<2.05 × 10 ⁻¹³	<13.7 × 10 ⁴⁰
2019 Sept 27	58753	<i>Chandra</i> ACIS-S	40.53	727	(1.28 ± 0.36) × 10 ⁻³	(2.87 ± 0.53) × 10 ⁻¹⁴	(1.94 ± 0.43) × 10 ⁴⁰
2021 May 03	59337	<i>Swift</i> -XRT	4.71	1310	<2.81 × 10 ⁻³	<1.48 × 10 ⁻¹³	<10.0 × 10 ⁴⁰

Note. For *Chandra* observations, the temperature was fixed to 3 keV (see Section 4). The best fit column density is $N_H = (1.13^{+0.78}_{-0.58}) \times 10^{22}$ cm⁻¹. The count rates have been converted to fluxes assuming a thermal plasma of 3 keV and column density of 1.1×10^{22} cm⁻¹ for the *Swift*-XRT observations.

Table 2. Spitzer IRAC observations of SN 2017hcc.

Quantity	Wavelength	Date of observations		
		2018 Oct 29.35 (MJD 58420.35)	2019 Apr 20.58 (MJD 58593.58)	2019 Nov 08.57 (MJD 58795.57)
AOR id		66120960	68799232	68799488
Epoch (d)		393	568	770
Apparent magnitude	3.6 μ m	12.97 ± 0.04	13.16 ± 0.05	13.52 ± 0.05
	4.5 μ m	12.49 ± 0.04	12.56 ± 0.04	12.81 ± 0.04
Absolute magnitude	3.6 μ m	−21.32 ± 0.19	−21.14 ± 0.19	−20.77 ± 0.19
	4.5 μ m	−21.80 ± 0.19	−21.73 ± 0.19	−21.48 ± 0.19
Flux density (μ Jy)	3.6 μ m	1818.72 ± 70.35	1533.79 ± 64.98	1097.13 ± 55.58
	4.5 μ m	1813.78 ± 71.83	1703.51 ± 69.03	1354.05 ± 62.36
vL_v (erg s ⁻¹)	3.6 μ m	(10.42 ± 0.40) × 10 ⁴¹	(8.90 ± 0.37) × 10 ⁴¹	(6.29 ± 0.32) × 10 ⁴¹
	4.5 μ m	(8.28 ± 0.33) × 10 ⁴¹	(7.78 ± 0.32) × 10 ⁴¹	(6.18 ± 0.28) × 10 ⁴¹
Dust mass ^a (M _⊕)		2.26 × 10 ^{−3}	3.60 × 10 ^{−3}	4.57 × 10 ^{−3}
Dust Temp (K)		1.28 × 10 ³	1.07 × 10 ³	0.93 × 10 ³
L_{bol} ^b (erg s ⁻¹)		4.80 × 10 ⁴¹	3.73 × 10 ⁴¹	2.70 × 10 ⁴¹
Blackbody radius (cm)		1.57 × 10 ¹⁶	1.97 × 10 ¹⁶	2.23 × 10 ¹⁶

Notes. ^aThe dust mass estimates are sensitive to the chosen grain parameters. The listed values are estimated assuming 1 μ m grain size of graphite composition.

^bBolometric luminosity assuming a single temperature dust blackbody radiation.

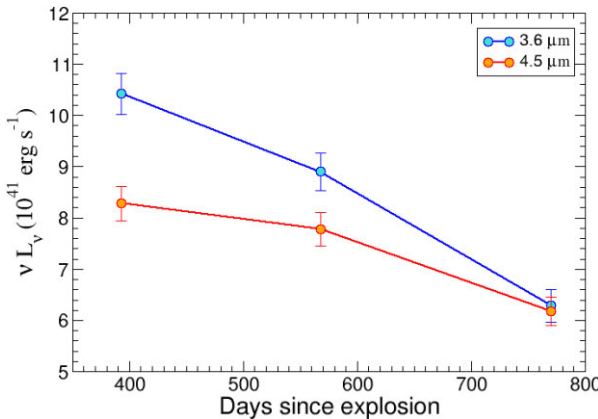


Figure 2. photometry of SN 2017hcc. The data are taken at 3 epochs [2018 Oct 29 (day 393), 2019 Apr 21 (day 568) and 2019 Nov 9 (day 770)] at 3.6 and 4.5 μ m wavelengths (Section 2.3). The temporal evolution indices at 3.6 μ m between days 393 and 568, and days 568 and 770 are -0.43 ± 0.15 , and -1.14 ± 0.22 , respectively. The temporal evolution indices at 4.5 μ m between days 393 and 568, and days 568 and 770 are -0.17 ± 0.16 , and -0.76 ± 0.20 , respectively.

2.5 VLA observations

The VLA observed SN 2017hcc between 2020 June 29–30 (MJD 59029–59030) in bands X (8–12 GHz) and K (18–26 GHz), and later in June 2021 in Ka (26–40 GHz), Ku (12–18 GHz), X, C (4–8 GHz), and S (2–4 GHz) bands. The data were analysed using the standard packages within the COMMON ASTRONOMY SOFTWARE APPLICATIONS package (CASA; McMullin et al. 2007). The details of the observations and the flux density values can be found in Table 3. We add 10 per cent error in the quadrature to the flux density values for analysis purposes, a typical uncertainty in the flux density calibration scale at the observed frequencies.⁴

3 ANALYSIS AND RESULTS

3.1 X-ray analysis and the column density

Swift-XRT observations of SN 2017hcc started when the SN was around a month old; however, the first X-ray detection of SN 2017hcc

⁴<https://science.nrao.edu/facilities/vla/docs/manuals/oss/performance/fdscale>

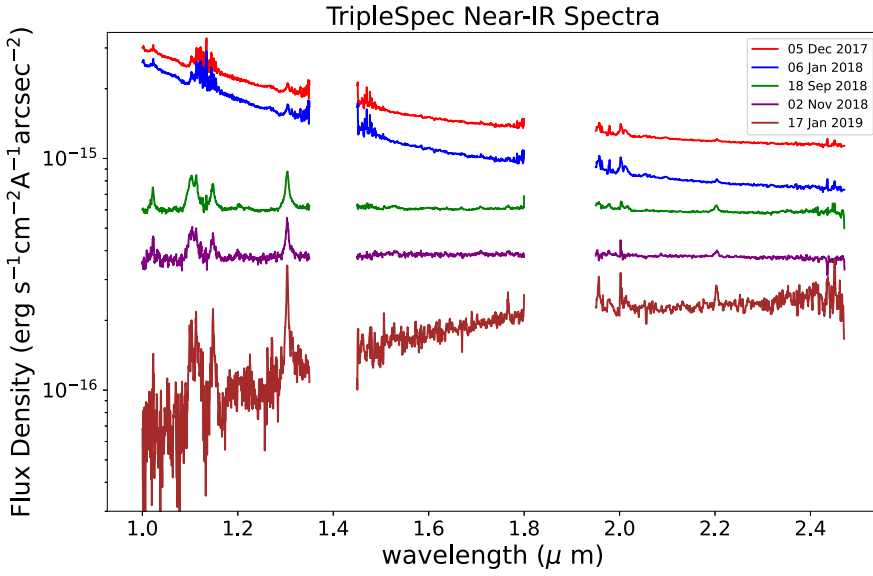


Figure 3. Triplespec near-IR spectra of SN 2017hcc on 2017 December 05 (day 66), 2018 January 06 (day 98), 2018 September 18 (day 353), 2018 November 02 (day 398) and 2019 January 17 (day 474). Note that the early spectra are brighter at lower wavelengths, whereas the late time spectra are brighter at longer wavelengths. To show this trend better, the top four spectra are offset by 10^{-15} , 6×10^{-16} , 5×10^{-16} , and 3×10^{-16} $\text{erg s}^{-1} \text{cm}^{-2} \text{A}^{-1} \text{arcsec}^{-2}$, respectively.

Table 3. Radio observations of SN 2017hcc.

Date of Obs. (UT)	MJD	Telescope	Age (days)	Central Freq (GHz)	Flux density μJy	rms μJy	Luminosity $(\text{erg s}^{-1} \text{Hz}^{-1})$	νL_ν (erg s^{-1})
2020 June 29	59029	VLA	1002	10.0	32.5 ± 7.6	6.7	$(2.19 \pm 0.51) \times 10^{26}$	$(2.19 \pm 0.51) \times 10^{36}$
2020 June 30	59030	VLA	1003	22.0	77.1 ± 16.2	15.5	$(5.19 \pm 1.09) \times 10^{26}$	$(11.42 \pm 2.40) \times 10^{36}$
2021 June 04	59369	VLA	1342	10.0	<45.6	15.26	$<3.07 \times 10^{26}$	$<3.07 \times 10^{36}$
2021 June 09	59374	VLA	1347	15.4	31.0 ± 11.3	10.5	$(2.09 \pm 0.76) \times 10^{26}$	$(3.21 \pm 1.17) \times 10^{36}$
2021 June 09	59374	VLA	1347	6.1	<26.7	8.9	$<1.80 \times 10^{26}$	$<1.10 \times 10^{36}$
2021 June 11	59376	VLA	1349	3.0	<182.4	60.7	$<12.28 \times 10^{26}$	$<3.68 \times 10^{36}$
2021 June 14	59379	VLA	1352	33.1	33.5 ± 11.8	11.6	$(2.26 \pm 0.79) \times 10^{26}$	$(7.46 \pm 2.63) \times 10^{36}$
2021 June 16	59381	VLA	1354	1.5	<228	76.1	$<15.34 \times 10^{26}$	$<2.30 \times 10^{36}$

was at an age of ~ 2 yr with the *Chandra* telescope. Our *Chandra* observations did not have enough counts to determine the shock temperature and the column density separately. We assumed a temperature of ~ 3 keV, corresponding to a CDS velocity of 1600 km s^{-1} , as advocated by Smith & Andrews (2020). The best fit column density is $1.13^{+0.78}_{-0.58} \times 10^{22} \text{ cm}^{-2}$ (Fig. 1). The Milky Way line of sight reddening is $E(B - V) = 0.0285$ and that through the host galaxy is $E(B - V) = 0.016$ (Smith & Andrews 2020). These values correspond to their respective column densities of $N_{H,\text{MW}} = 1.64 \times 10^{20} \text{ cm}^{-2}$ and $N_{H,\text{host}} = 0.92 \times 10^{20} \text{ cm}^{-2}$, using Schlafly & Finkbeiner (2011) recalibration of the Schlegel, Finkbeiner & Davis (1998) extinction map. To derive N_H , we use $N_H = E(B - V) \times 5.8 \times 10^{21} \text{ cm}^{-2}$. However, this relation is an empirical relation and has uncertainties (e.g. Gudennavar et al. 2012; Liszt 2019). Combining the column density due to the Milky Way and the host galaxy gives $2.56 \times 10^{20} \text{ cm}^{-2}$, which has negligible effect on the best fit column density which is two orders of magnitude higher. The excess column density comes from the CSM, i.e. $N_{H,\text{CSM}} = \sim 1.10 \times 10^{22} \text{ cm}^{-2}$.

The 0.3–10.0 keV unabsorbed flux is $f_{0.3-10\text{keV}} = (2.87 \pm 0.53) \times 10^{-14} \text{ erg cm}^{-2} \text{s}^{-1}$, corresponding to a luminosity of $L_{0.3-10\text{keV}} = (1.94 \pm 0.43) \times 10^{40} \text{ erg s}^{-1}$. This value does not change significantly even if we use an X-ray emitting plasma temperature of 20 keV based on the temperature observed in SN 2010jl (Ofek et al. 2014; Chandra et al. 2015). In Fig. 4, we plot

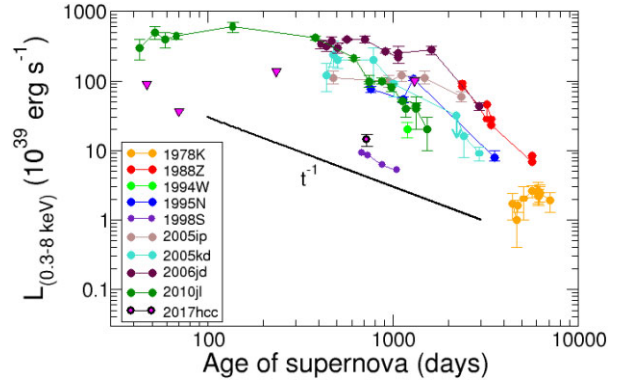


Figure 4. The 0.3–8 keV luminosities of X-ray detected SNe IIn. The *Chandra* SN 2017hcc detection is marked with a big magenta circle and the *Swift* upper limits with inverted triangles. Reproduced from Chandra (2018).

the SN 2017hcc X-ray luminosity along with other well-observed SNe IIn. Other than SN 1978K and SN 1998S, detected SNe IIn are brighter than SN 2017hcc. The SN 2017hcc luminosity is comparable to that of SN 1998S at the same age. We discuss the possible reasons for low X-ray luminosity in Section 4.

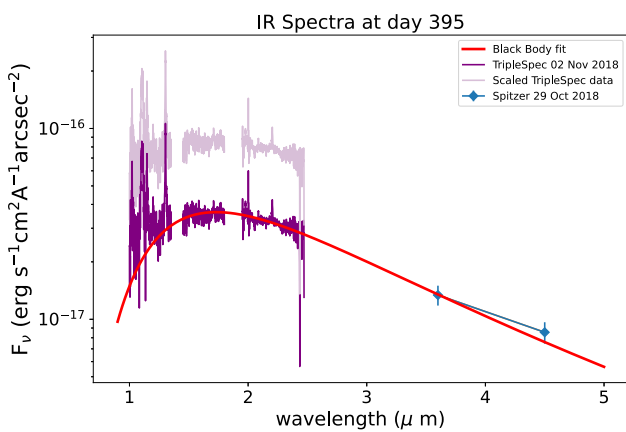


Figure 5. The spectra on day ~ 395 combined with TripleSpec and Spitzer data. The light purple colour shows original spectrum, whereas the purple spectrum has been shifted upwards to match the blackbody curve passing through the $3.6\text{ }\mu\text{m}$ *Spitzer* data point.

3.2 IR analysis

SN 2017hcc is extremely bright at *Spitzer* IRAC wavelengths. The $4.6\text{ }\mu\text{m}$ absolute magnitude reached -21.7 mag after a year, which corresponds to a peak IR luminosity $\sim 10^{42}\text{ erg s}^{-1}$. The late time emission is dominated by the IR emission (Smith & Andrews 2020), as is frequently the case for SNe IIn (see Section 1). We estimate the temporal evolution β (where β is defined as $F_\nu(t) \propto t^\beta$) and between *Spitzer* flux densities ($F_\nu(t)$) in μJy (Fig. 2). The temporal evolution between epochs 1 and 2, at 3.6 and $4.5\text{ }\mu\text{m}$, are $\beta = -0.46 \pm 0.16$ and $\beta = -0.17 \pm 0.15$, respectively. The temporal indices between the epochs 2 and 3 at the two frequencies are $\beta = -1.10 \pm 0.21$ and $\beta = -0.76 \pm 0.20$. The spectral indices α (defined as $F_\nu \propto \nu^\alpha$) between the two wavelengths at each epoch are $\alpha = -0.01 \pm 0.25$, $\alpha = 0.47 \pm 0.26$, and $\alpha = 0.94 \pm 0.31$, respectively. The slow decline of the IR emission, combined with the fast optical decline (Kumar et al. 2019; Smith & Andrews 2020), has important implications for the origin of the dust (Section 4.5).

The TripleSpec data at five epochs: 2017 December 5 (d 65), 2018 January 6 (d 97), September 18 (d 352), November 02 (d 397) and 2019 January 17 (d 473) are plotted in Fig. 3. While the early data are dominated by shorter wavelength emission, the later data reveal higher flux densities at longer wavelengths. A growing IR excess over the photospheric emission develops over time. We combine the measurements of *Spitzer* and TripleSpec on 2018 October 29 and 2018 November 2, respectively, and fit a simple blackbody model to the combined spectrum. The IR spectra using these data are plotted in Fig. 5. However, the calibration of the TripleSpec data has large uncertainties and hence the flux should not be considered absolute. Ideally it should be scaled to near-IR photometry. We have varied the scaling of the TripleSpec spectrum manually, and tried to shift to the blackbody curve passing through the Spitzer $3.6\text{ }\mu\text{m}$ data point. While the blackbody curve with $T \approx 1600\text{ K}$ fits the data reasonably well, there seems to be a slight excess of the $4.5\text{ }\mu\text{m}$ flux. However, the significance of the fit is low due to the calibration uncertainties and the fact that the scaled TripleSpec spectrum does not seem to go through both the Spitzer data points and that causes the uncertainty in the scaling factor. Hence, we do not use the parameters derived from these fits.

We compare the SN 2017hcc near-IR TripleSpec spectra with those of SN 2010jl in Fig. 6. The two SNe have qualitatively similar characteristics but there are significant differences. In SN 2017hcc,

the O I ($1.129\text{ }\mu\text{m}$) line is much stronger relative to Pa β ($1.282\text{ }\mu\text{m}$) than in SN 2010jl, while the He I ($1.083\text{ }\mu\text{m}$) line is weaker relative to Pa β . The H lines show some asymmetry towards the blue side in SN 2017hcc. This is seen visually as a greater area under the lines to the blue side of the central wavelength versus the red side. But the asymmetry is less than that in SN 2010jl. This could be due to dust formation in the post-shock shell and in the SN ejecta, which progressively obscures the redshifted part. Any associated CS dust was presumably evaporated by the SN. Narrow lines like those observed in SN 2010jl are present in SN 2017hcc (Smith & Andrews 2020) but are not resolved here. The width of the expected narrow lines is $\sim 50\text{ km s}^{-1}$, whereas the TripleSpec resolution is $\sim 100\text{ km s}^{-1}$. The estimated wind velocity is 100 km s^{-1} for SN 2010jl (Fransson et al. 2014), but is $40\text{--}50\text{ km s}^{-1}$ for SN 2017hcc (Smith & Andrews 2020).

3.3 Radio analysis

The VLA measurements show faint detections ($\leq 5\sigma$, as mentioned in Table 3 and Fig. 7). The peak spectral luminosity is $5.2 \times 10^{26}\text{ erg s}^{-1}\text{ Hz}^{-1}$, which is towards the lower end of the SNe IIn luminosities (Chandra 2018). The day 1000 spectral index between these frequencies is $+1.1$. This indicates that the supernova is still moderately optically thick. Such behaviour has been observed in the early evolution of other SNe IIn such as SN 1986J which showed $\alpha \sim +1.5$ in its rise to maximum (Weiler et al. 1990) and has been attributed to clumpiness in the emitting region (Weiler et al. 1990). Our radio data taken a year later show a higher radio luminosity. The spectral indices between the detected points are flat, indicating that the radio emission is near its transition from optically thick to thin regime. Due to the small number of data points, we fit the simple FFA model used in Chandra et al. (2012) assuming an optically thin spectral index of -0.6 . The best fits at the two epochs are shown in Fig. 7. We also attempt to fit the synchrotron self-absorption model (SSA) and from the peak we estimate the SSA velocity using the formulation in Chevalier (1998). This velocity is around $\sim 150\text{ km s}^{-1}$, which is an order of magnitude smaller than the ejecta velocity. This rules out SSA as a significant absorption mechanism.

4 DISCUSSION

4.1 Shock breakout in pre-supernova mass-loss

With a peak bolometric luminosity of $1.3 \times 10^{44}\text{ erg s}^{-1}$ reached in $\sim 30\text{ d}$ and an absolute magnitude of -20.7 mag (Prieto et al. 2017), SN 2017hcc is at the boundary of superluminous SNe with a two orders of magnitude larger luminosity than normal core-collapse SNe. In addition, strong narrow lines are present (Smith & Andrews 2020), indicating that dense outflowing CS gas surrounds the supernova. If this gas is sufficiently optically thick, the shock breakout radiation from the supernova will occur after the interaction shell has moved to the mass-loss region. Quantitatively, if the wind optical depth is τ_w and v_{sh} is the shock speed, then for cases where $\tau_w > c/v_{sh}$, the SN shock breaks out in the wind. Such a breakout through the thick wind may extend long enough, lasting days to months, and may account for the peak SN luminosity of SN 2017hcc (Chevalier & Irwin 2011).

We use the approximate formulation of Chevalier & Irwin (2011) for shock breakout in a wind. An initial assumption for this is that the mass-loss density profile is that for a steady wind, $\rho = Dr^{-2}$, where $D = \dot{M}/(4\pi R^2 v_w)$. As per their formulation, there are two

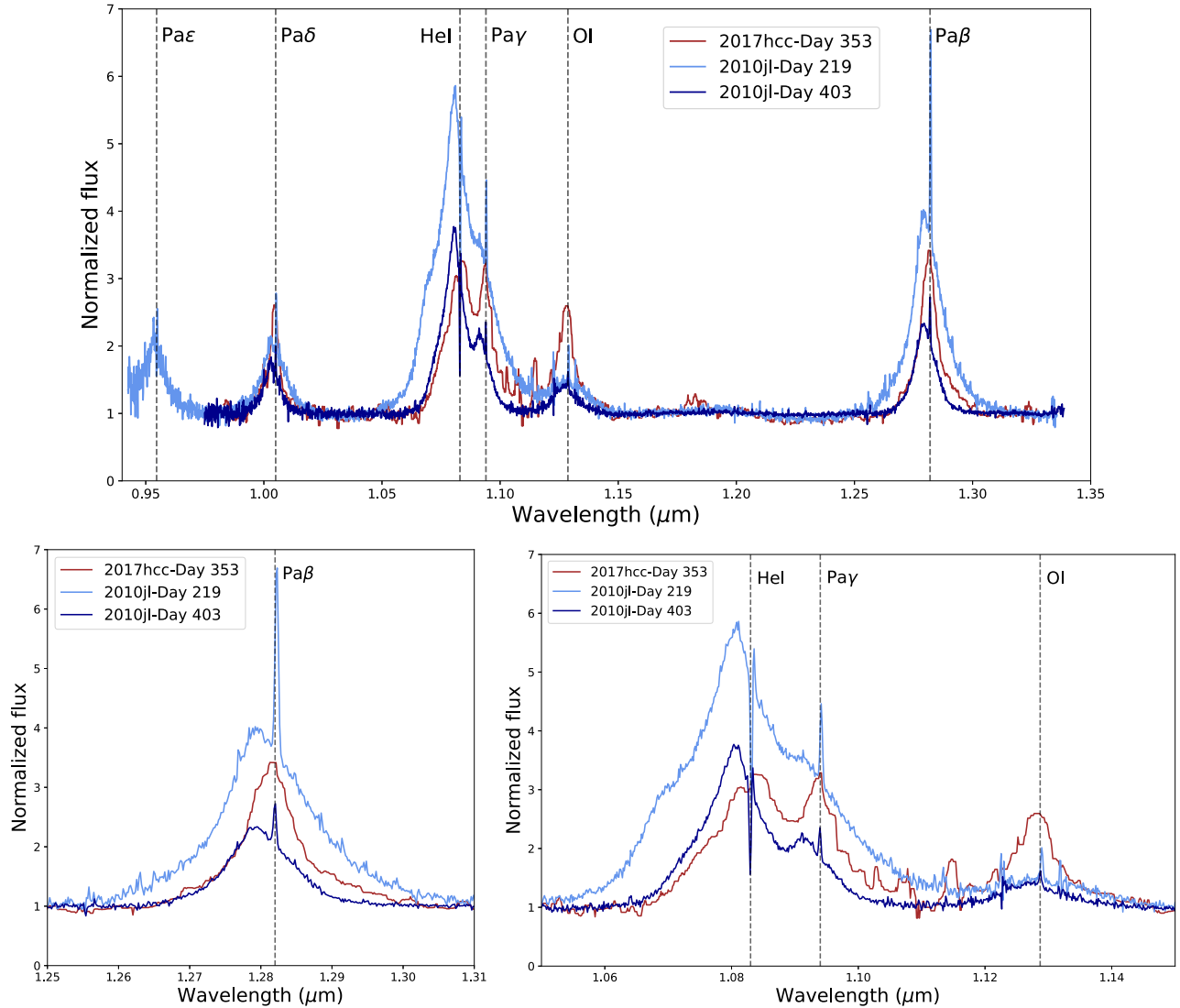


Figure 6. Comparison of near-IR spectra of SN 2017hcc (Borish et al. 2015) with those of SN 2010jl. Spectra are normalized to the continuum level. The SN 2017hcc spectrum is on day 353 [brown lines, corresponding to Triplesec data on 2018 September 18 (MJD 58379)]. SN 2010jl spectra are on day 219 (light blue lines) and day 403 (dark blue lines). Top panel: The full spectra. Bottom two panels show zoomed plots for O I, Pa β , Paschen γ , and He I lines.

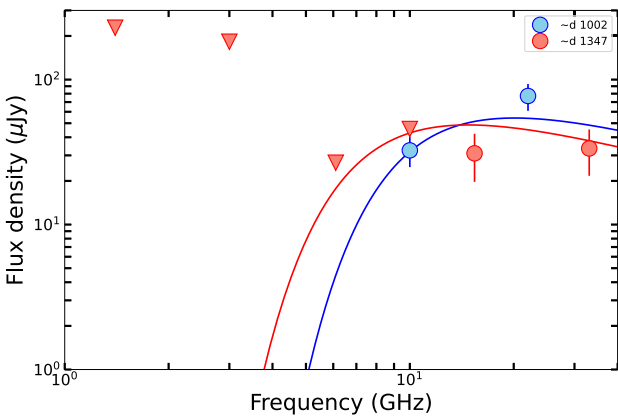


Figure 7. Radio spectra of SN 2017hcc with the VLA at two epochs. The spectra on day 1000 is in blue colour and the one on day 1347 is in red colour. The triangles represent upper limits. A simple FFA model is fit to the data.

length-scales that are important. One, R_d , is the radius at which the diffusion time equals the expansion time, so photons can move out through the wind. We have $R_d = \kappa D v_{sh}/c$, where κ is the opacity. The other important length-scale is R_w where the wind density cuts off. The character of the shock breakout is expected to depend on whether $R_w > R_d$, when the diffusion is important, or vice versa for which the diffusion time-scales are large (Chevalier & Irwin 2011). The indications are that SN 2017hcc is in the case $R_w > R_d$. This is indicated by the presence of bright IR emission to late times (2 yr) implying that the mass-loss region extends to large radius. Also, the narrow line emission in optical bands (Smith & Andrews 2020) shows a dense mass-loss region. We scale the parameter D to D_* such that $D_* = D/(5 \times 10^{16} \text{ g cm}^{-1})$ corresponding to a mass-loss rate of $0.1 M_\odot \text{ yr}^{-1}$ and wind velocity of 100 km s^{-1} . Here D is in g cm^{-1} and D_* is a dimensionless quantity. As mentioned earlier, in SN 2017hcc the rise time can be approximated by the rise time of the bolometric light curve, 30 d (Prieto et al. 2017), so $D_* \approx 4.5$. For the wind velocity of 45 km s^{-1} , we get $\dot{M} = 0.1 M_\odot \text{ yr}^{-1}$ which should apply near the time of maximum light.

At shock breakout, a radiation dominated shock can no longer be maintained and a CDS forms at the shock interface. A simple model for a supernova density profile, used by Chevalier & Irwin (2011), is an inner region with a flat density surrounded by a steep $\rho \propto r^{-7}$ profile. For typical parameters, the interaction region between the ejecta and the CSM is in the steep power-law region. For normal supernova parameters, equation (6) in Chevalier & Irwin (2011) shows that the breakout luminosity can be close to that observed in SN 2017hcc near bolometric peak.

In the above we use 4000 km s^{-1} for the shock velocity, as indicated in the X-ray observations of SN 2010jl (Chandra et al. 2015) and SN 2014C (Margutti et al. 2017). Here we discuss the shock velocity. Smith & Andrews (2020) determine v_{sh} from the emission line profiles of $\text{H}\alpha$ and $\text{H}\beta$. They find that the line profiles can be fit by 2 Gaussian components, one with a FWHM (full width at half-maximum) of 4000 km s^{-1} and one with 1100 km s^{-1} , which they identify with emission from the freely expanding ejecta and the CDS, respectively. After allowance for a geometrical factor, Smith & Andrews (2020) use 1600 km s^{-1} for v_{CDS} , where $v_{\text{CDS}} = v_{\text{sh}}$ for a thin shell. However, there is no clear physical reason for the emission from the CDS or ejecta to have a Gaussian profile with a width corresponding to a physical parameter. Dessart, Audit & Hillier (2015) modelled the emission from SN 2010jl and found reasonable estimates for the line profile of $\text{H}\alpha$ considering emission from the CDS with electron scattering and CDS velocity $\sim 3000 \text{ km s}^{-1}$. Also, in a spherically symmetric interaction, a large, unexpected deceleration would be required between the ejecta and the CDS for the values mentioned by Smith & Andrews (2020). In the formation of a thin shell between ejecta with power-law index n and CSM with power-law s , we have $R \propto t^{(n-3)/(n-s)}$ (Chevalier 1982) so that $v_{\text{ej}}/v_{\text{CDS}} = (n-s)/(n-3)$. For typical values $n = 8$ and $s = 2$ (e.g. Fransson et al. 2014, for SN 2010jl), we have $v_{\text{ej}}/v_{\text{CDS}} = 1.2$, as opposed to $v_{\text{ej}}/v_{\text{CDS}} = 2.50$ from the line observations (Smith & Andrews 2020). The low value of v_{CDS} is not consistent with the type of evolution seen in SN 2010jl during the first year if there is spherically symmetric expansion. Other estimates for v_{CDS} can be considered. In the case of SN 2010jl, an X-ray observation at 2 yr with NuSTAR showed a temperature of 20 keV (Ofek et al. 2014; Chandra et al. 2015), which corresponds to a shock velocity of 4000 km s^{-1} . A higher velocity would be expected at earlier times and there is possible evidence for a higher velocity from a feature that appears in the He I line in SN 2010jl (Borish et al. 2015; Chandra et al. 2015). We consider both small and large values for v_{CDS} .

For the shock front to break out in the wind region, $\tau_w > c/v_{\text{sh}}$ is needed. Taking R_b to be the radius of the base of the wind, we have $\tau_w \approx 5 \times 10^{16} k R_b^{-1} D_*$, where k is the opacity κ in units of $0.34 \text{ cm}^2 \text{ g}^{-1}$ (Chevalier & Irwin 2011). As discussed above, for $D_* = 4.5$, this gives $\tau_w \approx 76(R_b/10^{15} \text{ cm})^{-1}$. Thus for reasonable parameters, the shock breakout does occur in the wind.

One aspect of shock breakout is that the temperature should increase with rising luminosity, since the initial rise to maximum luminosity should be primarily due to heating of the photosphere. This has not been seen in SN 2017hcc (Kumar et al. 2019). However, we note that the early measurements for temperature are not available before the peak in the light curve.

4.2 Post-breakout interaction

Once the diffusion time is less than the supernova age, the luminosity corresponds to the power generated at the shock. We have a luminosity $L = 4\pi R^2 \epsilon \frac{1}{2} \rho v_{\text{sh}}^3$, where R is the radius of the CDS and ϵ is an efficiency factor for the conversion of shock power to

radiation (Chugai 1990). At early times, the cooling time is less than the age so the shock power is radiated and $\epsilon \approx 1$. With sufficient good quality data, the winds of SNe IIn are generally found to be not steady (Dwarkadas 2007), but the assumption should lead to a rough estimate for \dot{M} , which, for a steady wind is:

$$\dot{M} = 2L v_w / \epsilon v_{\text{sh}}^3. \quad (1)$$

The value of v_w can be estimated from high spectral resolution observations. Smith & Andrews (2020) find $v_w \approx (40-50) \text{ km s}^{-1}$. To estimate the value of \dot{M} , we use the bolometric luminosity of $\sim 10^{42} \text{ erg s}^{-1}$ which is the luminosity of IR dust emission at $1-2 \text{ yr}$ (Table 2). We now find from equation (1) $\dot{M} = 2 \times 10^{-3} \epsilon^{-1} L_{42} (v_{\text{sh}}/4000 \text{ km s}^{-1})^{-3} \text{ M}_\odot \text{ yr}^{-1}$, where $v_w = 45 \text{ km s}^{-1}$ is assumed, and L_{42} is the bolometric luminosity in the units of $10^{42} \text{ erg s}^{-1}$. So we now have $D_* \approx 0.024$. We note that the value of v_w is determined over the first 100 d (Smith & Andrews 2020); there could be a change at later times. In addition, the value of the mass-loss is sensitive to the shock velocity. However, our results indicate that the mass-loss density drops more rapidly with radius than in the steady (r^{-2}) case.

The cooling of the post-shock gas is important for the value of ϵ in the above formula. We now discuss the validity of cooling. Our discussion is similar to that of Chevalier & Fransson (2017). For electron temperature $T_e \gtrsim 2.6 \times 10^7 \text{ K}$, which is expected for the post-forward shock wave, free-free cooling dominates with a cooling rate $\Lambda = 1.0 \times 10^{-23} (T_e/10^7 \text{ K})^{0.5} \text{ erg s}^{-1} \text{ cm}^3$. Assuming isobaric cooling behind the shock, the cooling time is $t_{\text{cool}} = 5kT_e/n_H\Lambda(T_e)$. Using Chevalier & Fransson (2017) equation (18), the transition time at which the age equals the cooling time, for ejecta velocity 4000 km s^{-1} (indicated with $v_{\text{ej},4}$ in the formula below) is (for $n = 8$)

$$t_{\text{tr}} = 342 D_* v_{\text{ej},4}^{-3} \text{ d}, \quad (2)$$

which is 75 d for our preferred parameters. This estimate would imply that the supernova was past the cooling phase at the time of the X-ray observation. However, the uncertainties are large so some effect of cooling cannot be ruled out. The estimates should be taken with caution, since the properties of the absorbing gas are uncertain because of early Compton heating and radiative cooling as well as recombination (Lundqvist & Fransson 1988).

4.3 Variable mass-loss rate

The above treatment shows that the mass-loss rate obtained at $\sim 30 \text{ d}$ from the shock breakout was $\sim 0.1 \text{ M}_\odot \text{ yr}^{-1}$, whereas at few hundred days, obtained from the IR measurements, was $\sim 2 \times 10^{-3} \text{ M}_\odot \text{ yr}^{-1}$. In addition, we can also use the timing of the peak radio flux density to estimate the mass-loss rate at $\sim 1000 \text{ d}$. The mass-loss rate derived from our radio measurement assuming a CSM temperature of 10^4 K is $\sim 6.5 \times 10^{-4} \text{ M}_\odot \text{ yr}^{-1}$.

These epochs correspond to roughly ~ 10 , ~ 100 , and $\sim 300 \text{ d}$ before explosion and the mass-loss rate changes roughly two to three orders of magnitude. This indicates a variable mass-loss rate, with enhanced mass-loss event occurring a decade before the supernova explosion.

There is a growing number of evidence that many core-collapse supernovae undergo similar enhancements during the last years before the explosion. Maeda et al. (2021) reported evidence of enhanced mass-loss in nearby type Ic supernova SN 2020oi in their Atacama Large Millimeter Array (ALMA) observations, which they interpreted as the pre-SN activity likely driven by the nuclear burning activities in the star's final moments. Similar conclusions were drawn for the famous supernova SN 2014C undergoing metamorphosis

from a stripped envelope supernova to a Type IIn via their radio and X-ray observations (Anderson et al. 2017; Margutti et al. 2017; Brethauer et al. 2022). The flash spectroscopy of various supernovae have also revealed the similar conclusions. A remarkable example is SN 2013fs, discovered mere 3 h after the explosion by the automated real-time discovery and classification pipeline of the intermediate Palomar Transient Factory (iPTF) survey, which enabled spectroscopy measurements within 6 h of discovery (Yaron et al. 2017). The early measurements revealed a dense CSM to be confined within 10^{15} cm indicating enhanced mass-loss ($10^{-3} M_{\odot} \text{ yr}^{-1}$) in the last one year before explosion in an otherwise normal core-collapse supernova. This led authors to suggest that such pre-SN activities may be common in exploding stars. Shivvers et al. (2015) examined the Keck HIRES spectrum of SN 1998S taken within a few days after the SN and found convincing evidence for enhanced mass-loss rate in the last 15 yr of star’s life. These measurements combined with other published measurements indicated much smaller mass-loss rate at earlier times, arriving at the conclusion of this section. SN 2020tlf was a normal Type IIP/IIL supernova, where flash spectroscopy soon after the discovery revealed evidence of photoionization of CSM confined within 10^{15} cm created at a mass-loss rate of $10^{-2} M_{\odot} \text{ yr}^{-1}$ in a $10-12 M_{\odot}$ red supergiant progenitor, whereas 3 orders of magnitude smaller mass-loss rate at larger distances (Jacobson-Galán et al. 2022). Similarly Terreran et al. (2022) also found the presence of dense and confined CSM indicating a phase of enhanced mass-loss in its final moments of the progenitor of SN 2020pni. Tartaglia et al. (2021) presented the very early phase to nebular phase observations of Type II supernova SN 2017ahn, discovered just a day after explosion. Their modelling indicated a complex CSM surrounding the progenitor star with evidence of enhanced mass-loss in the last moments of likely massive yellow supergiant progenitor. While for SNe IIn, LBV scenario has been favoured for enhanced mass-loss rates just before the explosion, above examples favour the idea that many core-collapse supernovae of different flavours may experience enhanced mass-loss in their final years, which could be governed by somewhat common physical mechanisms (Terreran et al. 2022).

4.4 Low X-ray luminosity

The lack of bright X-rays in SN 2017hcc is surprising, as the detected SNe IIn are generally brighter than other core-collapse supernovae (Chandra 2018). A dense interaction is indicated in SN 2017hcc at early epochs by the optical luminosity and electron scattering line profiles. X-ray emission is detected at day 700 but the luminosity of SN 2017hcc is lower than that typically found for strongly interacting supernovae of Type IIn and is closer to the luminosity observed from SN 1998S (Fig. 4). In SN 2017hcc during the time of the *Chandra* observation, most of the shock power goes into the IR, which is $\sim 10^3$ times the X-ray emission at the same epoch. SN 1998S had late IR emission, but at a level $\sim 10^{40} \text{ erg s}^{-1}$ (Pozzo et al. 2005) at 2 yr, which is nearly two orders of magnitude smaller than that of SN 2017hcc; the lower luminosity was consistent with the lower mass-loss rate of $2 \times 10^{-4} M_{\odot} \text{ yr}^{-1}$ deduced from the radio and X-ray emission (Pooley et al. 2002).

When the interaction is strong, the forward shock front is initially radiative and evolves to a non-radiative phase (Chevalier & Irwin 2012). In the cooling phase, the CDS created by the interaction is subject to the non-linear thin shell instability (NTSI), giving rise to a corrugated structure (Vishniac 1994). Numerical simulations of the instability show that the X-ray emission is suppressed (Kee, Owocki & ud-Doula 2014; Steinberg & Metzger 2018). The reason

for X-ray suppression is the CDS that forms. The hot post-shock gas cools radiatively towards lower temperature and pressure in the presence of the CDS. Much of the cool emitting gas is underpressured relative to the hot surrounding medium. This pressure difference between the hot shock and the cool dense shell robs the hot gas of its thermal energy, which is now radiated with high efficiency at lower temperature. Another factor is that the corrugation of the forward shock gives oblique shocks that are weaker than head on shocks. However, as discussed above, estimates of the cooling at the time of the X-ray detection indicates that the shockwave is probably not cooling. In this case, the NTSI is not a factor, although the uncertainties and assumptions may allow the cooling scenario.

4.5 Late time excess of IR emission and origin of the dust

The *Spitzer* IR photometric data corresponds to peak IR luminosities reaching $\sim 10^{42} \text{ erg s}^{-1}$.

The origin of the bright IR emission at late times is not clear. The IR evolution is rather flat, as opposed to a faster decline seen in the optical band (Kumar et al. 2019), though at earlier times. Usually, the IR excess implies a rising relative contribution of the dust component to the bolometric luminosity as the optical light-curve fades. The late-time high IR luminosity and the systematic blueshift in the line profiles (Smith & Andrews 2020) suggest that SN 2017hcc likely has contributions from two components: 1) dust formation in the ejecta and the CDS, and 2) pre-existing dust beyond the evaporation radius, giving rise to IR emission.

Smith & Andrews (2020) find that SN 2017hcc line profiles show a progressively increasing blueshift. They reject the possibility of this feature being due to occultation by the SN photosphere, pre-shock acceleration of the CSM, or asymmetric CSM, and explain it to be arising due to absorption by newly formed dust in the post-shock shell and then SN ejecta.

Based on our IR fits, we can calculate the blackbody radius, r_{bb} , which is the minimum size of the dust emitting component, using the modified blackbody expression given in Fox et al. (2010). Using the best fit values in Table 2, the bolometric luminosities assuming blackbody emission are $4.79 \times 10^{41} \text{ erg s}^{-1}$, $3.73 \times 10^{41} \text{ erg s}^{-1}$, and $2.70 \times 10^{41} \text{ erg s}^{-1}$ at epochs 393, 568, and 770 d, respectively.

These luminosities imply that the values of r_{bb} are $1.6 \times 10^{16} \text{ cm}$, $2 \times 10^{16} \text{ cm}$, and $2.2 \times 10^{16} \text{ cm}$ at these epochs, respectively. The shock radii at these epochs are $(0.5 - 1.3) \times 10^{16}$, $(0.8 - 2.0) \times 10^{15}$, and $(1.1 - 2.7) \times 10^{16} \text{ cm}$, respectively for shock velocity ranging between $1600-4000 \text{ km s}^{-1}$. We note that these values have significant uncertainties arising from assumption of single graphite grain of size $1 \mu\text{m}$ and a single temperature, as well as due to uncertainties in the opacity measurements. These findings give interesting clues to the dust origin. The shock can typically destroy any pre-existing dust within the shock radius. The shock radii are smaller (or equal for higher ejecta velocity) than the blackbody radii at each epoch. This implies that there could still be pre-existing dust that is beyond the outer shock front that can give the IR emission (Fox et al. 2011), in addition to newly formed dust and can cause IR excess.

The dust luminosity of SNe IIn in general is higher than in other SNe, suggesting that the dense CSM is important for dust formation in strongly interacting SNe IIn (Tinianont et al. 2016). However, most of the SNe IIn with a high IR flux were also associated with a high X-ray luminosity. This is not the case with SN 2017hcc. Fig. 4 shows the SN 2017hcc X-ray luminosity with other well observed SNe IIn. Other than SN 1978K and SN 1998S, the detected SNe IIn are brighter than SN 2017hcc. The luminosity of SN 2017hcc is

comparable to that of SN 1998S at the same age, which is known to be due to lower CS interaction. This is unlikely to be the case for SN 2017hcc.

4.6 Asymmetry in the CSM

Asymmetry has been seen in many SNe IIn. For example, the large X-ray luminosity of SN 2006jd implied a high density, but a small amount of photoabsorption in the spectrum implied a low density (Chandra et al. 2012). These conflicting measurements suggested an asymmetric CSM. This seems to be a general feature of interacting CSM, and may indirectly support the LBV progenitor scenario (Smith 2014).

Direct evidence for asymmetry in SN 2017hcc comes from measurements of high polarization of the photospheric emission (Mauerhan et al. 2017; Kumar et al. 2019). The fact that the polarized fraction declined with time indicates that the asymmetry was in the CSM, not the supernova ejecta.

Also, Smith & Andrews (2020) found, based on blueshifted line profiles, that the intrinsic emission line profile from the fast SN ejecta is symmetric, suggesting that the underlying SN explosion itself was not highly aspherical, and the polarization is likely related to the CSM. Another line of argument regarding the highly asymmetric CSM in SN 2017hcc suggests that the polarization measurements are close to maximum. The emission at maximum light in SNe IIn is dominated by interaction of the ejecta with the CSM, implying that the major source of intrinsic polarization at maximum is due to this interaction, particularly with an asymmetric CSM. The luminosity from the interaction becomes progressively weaker as the CSM around the SN evolves into an optically thin state, resulting in a decrease in polarization.

In addition, Smith & Andrews (2020) find that even though optical depths of the CSM are quite high, the SN ejecta emerge by day 75, which requires a non-spherical geometry of the CSM.

Smith & Andrews (2020) noted that the line profiles during the first ~ 100 d are remarkably symmetric, indicating that the CSM speed remains similar over a large range of radii regardless of the changing supernova luminosity. The observed asymmetry at later times is mild and limited to low radial velocities. Based on these two arguments, they suggested that the asymmetry is in the form of axisymmetry and our line of sight is close to the polar region, which when viewed from the Earth at an intermediate latitude will show asymmetry.

As the main power source for SNe IIn is the kinetic energy of the SN ejecta, a large fraction of the ejecta kinetic energy can be converted into radiation due to the high density CSM. However, an axisymmetric CSM could lead to an inefficient conversion of kinetic energy into radiation in some directions, causing a lower X-ray flux. A low column density can be explained by the axisymmetry. Our radio measurements may also support this view. The radio flux is very faint which may indicate absorption of the flux. Thus, it is possible that the bright IR is arising from the same region, which may be more symmetric and is different from the region where low luminosity radio and X-rays arise (see fig. 14 of Smith & Andrews 2020). In this scenario, the X-rays are completely absorbed in the region of high luminosity and the observed X-rays are from a region of weak interaction with relatively lower column density.

5 SUMMARY AND CONCLUSIONS

SN 2017hcc had one of the highest bolometric luminosities for a SN IIn, but low X-ray and radio luminosities. The peak bolometric

luminosity of $\sim 10^{44}$ ergs s $^{-1}$ (Prieto et al. 2017) is likely to be due to CS interaction. During the first 100 d, there are only upper limits on the X-ray luminosity, $< 3 \times 10^{40}$ ergs s $^{-1}$, so the ratio of X-ray to total luminosity is < 0.0003 . These results are comparable to those observed in SN 2006gy (Ofek et al. 2007; Smith et al. 2007). SN 2017hcc has properties that are consistent with shock breakout in a dense wind (Chevalier & Irwin 2011).

The optical/IR lines during the first 100 d show electron scattering profiles that require an electron scattering optical depth of at least a few, which corresponds to a column density of at least 10^{24} cm $^{-2}$. Our early time *Swift*-XRT measurements result in a non-detection; hence, we are unable to constrain the column depth. It is possible that the early X-rays were absorbed due to the high column density. Shock breakout in a dense medium also results in suppression of X-ray emission. In addition, the non-linear thin-shell instability due to a radiative forward shock results in further suppression of the X-rays.

There is a late time enhancement in the IR emission with peak IR luminosities reaching $\sim 10^{42}$ erg s $^{-1}$. At the same epoch, the X-ray luminosity is two orders of magnitude lower. We interpret the high IR luminosity as likely due to contributions from new dust as well as old dust.

We also show that SN 2017hcc likely underwent a phase of enhanced mass-loss years before explosion. This has been seen in many SNe IIn and may indirectly support an LBV scenario, though the fine tuning between an LBV undergoing enhanced mass-loss and SN explosion remains an important issue. Thus SN 2017hcc adds an important input towards our understanding of highly interacting SNe, whose progenitors remain a mystery.

ACKNOWLEDGEMENTS

We thank the referee for useful comments, which helped improve the manuscript. RAC acknowledges support from NASA through Chandra award number GO0-21054X issued by the Chandra X-ray Center and from NSF grant AST-1814910. PC acknowledges support of the Department of Atomic Energy, Government of India, under project number 12-R&D-TFR-5.02-0700. The Chandra Center is operated by the Smithsonian Astrophysical Observatory for and on behalf of NASA under contract NAS8-03060. The National Radio Astronomy Observatory is a facility of the National Science Foundation operated under cooperative agreement by Associated Universities, Inc. This research has made use of data and/or software provided by the High Energy Astrophysics Science Archive Research Center (HEASARC), which is a service of the Astrophysics Science Division at NASA/GSFC. This work is based (in part) on observations made with the Spitzer Space Telescope, which was operated by the Jet Propulsion Laboratory, California Institute of Technology under a contract with NASA. Support for this work was provided by NASA. This work made use of data supplied by the UK Swift Science Data Centre at the University of Leicester.

DATA AVAILABILITY

The data underlying this article will be shared upon a reasonable request to the corresponding author.

REFERENCES

Anderson G. E. et al., 2017, *MNRAS*, 466, 3648
 Andrews J. E., Smith N., McCully C., Fox O. D., Valenti S., Howell D. A., 2017, *MNRAS*, 471, 4047

Arnaud K. A., 1996, in Jacoby G. H., Barnes J., eds, ASP Conf. Ser. Vol. 101, Astronomical Data Analysis Software and Systems V. Astron. Soc. Pac., San Francisco, p. 17

Bak Nielsen A.-S., Hjorth J., Gall C., 2018, *A&A*, 611, A67

Bevan A. M. et al., 2020, *ApJ*, 894, 111

Borish H. J., Huang C., Chevalier R. A., Breslauer B. M., Kingery A. M., Privon G. C., 2015, *ApJ*, 801, 7

Brethauer D. et al., 2022, preprint ([arXiv:2206.00842](https://arxiv.org/abs/2206.00842))

Cash W., 1979, *ApJ*, 228, 939

Chandra P., 2018, *Space Sci. Rev.*, 214, 27

Chandra P., Chevalier R. A., Chugai N., Fransson C., Irwin C. M., Soderberg A. M., Chakrabarti S., Immler S., 2012, *ApJ*, 755, 110

Chandra P., Chevalier R. A., Chugai N., Fransson C., Soderberg A. M., 2015, *ApJ*, 810, 32

Chandra P., Chevalier R. A., Chugai N., Milisavljevic D., Fransson C., 2020, *ApJ*, 902, 55

Chevalier R. A., 1982, *ApJ*, 259, 302

Chevalier R. A., 1998, *ApJ*, 499, 810

Chevalier R. A., Irwin C. M., 2011, *ApJ*, 729, L6

Chevalier R. A., Irwin C. M., 2012, *ApJ*, 747, L17

Chevalier R. A., Fransson C., 2017, in Alsabti A., Murdin P., eds, Supernova Handbook. Springer, New York, p. 875

Chugai N. N., 1990, Pis'ma Astron. Zh., 16, 1066

Chugai N. N., 2001, *MNRAS*, 326, 1448

Cushing M. C., 2004, PhD thesis, Univ. Hawai'i

Dessart L., Audi E., Hillier D. J., 2015, *MNRAS*, 449, 4304

Draine B. T., Lee H. M., 1984, *ApJ*, 285, 89

Dwarkadas V. V., 2007, *Ap&SS*, 307, 153

Dwarkadas V. V., Gruszk J., 2012, *MNRAS*, 419, 1515

Dwek E., Sarangi A., Arendt R. G., Kallman T., Kazanas D., Fox O. D., 2021, *ApJ*, 917, 84

Elias-Rosa N. et al., 2018, *ApJ*, 860, 68

Fassia A. et al., 2000, *MNRAS*, 318, 1093

Fazio G. G. et al., 2004, *ApJS*, 154, 10

Fox O. D. et al., 2011, *ApJ*, 741, 7

Fox O. D., Chevalier R. A., Dwek E., Skrutskie M. F., Sugerman B. E. K., Leisenring J. M., 2010, *ApJ*, 725, 1768

Fox O. et al., 2009, *ApJ*, 691, 650

Fransson C. et al., 2014, *ApJ*, 797, 118

Fruscione A. et al., 2006, SPIE Conf. Ser. Vol. 6270, Observatory Operations: Strategies, Processes, and Systems. SPIE, Bellingham, p. 62701V

Gall C. et al., 2014, *Nature*, 511, 326

Gerardy C. L. et al., 2002, *ApJ*, 575, 1007

Gerardy C. L., Fesen R. A., Höflich P., Wheeler J. C., 2000, *AJ*, 119, 2968

Gudennavar S., sg B., Krishnamoorthy P., Murthy J., 2012, *ApJS*, 199, 8

Jacobson-Galán W. V. et al., 2022, *ApJ*, 924, 15

Kee N. D., Owocki S., ud-Doula A., 2014, *MNRAS*, 438, 3557

Kiewe M. et al., 2012, *ApJ*, 744, 10

Kumar B. et al., 2019, *MNRAS*, 488, 3089

Liszt H., 2019, *ApJ*, 881, 29

Lundqvist P., Fransson C., 1988, *A&A*, 192, 221

Maeda K. et al., 2021, *ApJ*, 918, 34

Margutti R. et al., 2014, *ApJ*, 780, 21

Margutti R. et al., 2017, *ApJ*, 835, 140

Mauerhan J. C., Filippenko A. V., Brink T. G., Zheng W., 2017, Astron. Telegram, 10911, 1

Mauerhan J., Smith N., 2012, *MNRAS*, 424, 2659

McMullin J. P., Waters B., Schiebel D., Young W., Golap K., 2007, in Shaw R. A., Hill F., Bell D. J., eds, ASP Conference Series, Vol. 376, Astronomical Data Analysis Software and Systems XVI. Tucson, Arizona, USA, p. 127

Nayana A. J., Chandra P., 2017, Astron. Telegram, 11015, 1

Ofek E. O. et al., 2007, *ApJ*, 659, L13

Ofek E. O. et al., 2014, *ApJ*, 788, 154

Pooley D. et al., 2002, *ApJ*, 572, 932

Pozzo M., Meikle W. P. S., Fassia A., Geballe T., Lundqvist P., Chugai N. N., Sollerman J., 2005, in Turatto M., Benetti S., Zampieri L., Shea W., eds, ASP Conf. Ser. Vol. 342, 1604-2004: Supernovae as Cosmological Lighthouses. Astron. Soc. Pac, San Francisco, p. 337

Prieto J. L. et al., 2017, *Res. Notes Am. Astron. Soc.*, 1, 28

Sarangi A., Dwek E., Arendt R. G., 2018, *ApJ*, 859, 66

Schlafly E. F., Finkbeiner D. P., 2011, *ApJ*, 737, 103

Schlegel D. J., Finkbeiner D. P., Davis M., 1998, *ApJ*, 500, 525

Schlegel E. M., 1990, *MNRAS*, 244, 269

Shappee B. J. et al., 2014, *ApJ*, 788, 48

Shivvers I., Groh J. H., Mauerhan J. C., Fox O. D., Leonard D. C., Filippenko A. V., 2015, *ApJ*, 806, 213

Smith N. et al., 2007, *ApJ*, 666, 1116

Smith N. et al., 2009, *ApJ*, 695, 1334

Smith N., 2014, *ARA&A*, 52, 487

Smith N., Andrews J. E., 2020, *MNRAS*, 499, 3544

Smith N., Foley R. J., Filippenko A. V., 2008, *ApJ*, 680, 568

Smith N., Owocki S. P., 2006, *ApJ*, 645, L45

Steinberg E., Metzger B. D., 2018, *MNRAS*, 479, 687

Stritzinger M. et al., 2012, *ApJ*, 756, 173

Svirski G., Nakar E., Sari R., 2012, *ApJ*, 759, 108

Szalai T. et al., 2021, *ApJ*, 919, 17

Tartaglia L. et al., 2021, *ApJ*, 907, 52

Terreran G. et al., 2022, *ApJ*, 926, 20

Tinyanont S. et al., 2016, *ApJ*, 833, 231

Tony J. L., 2011, *PASP*, 123, 58

Trundle C. et al., 2009, *A&A*, 504, 945

Van Dyk S. D., 2013, *AJ*, 145, 118

Van Marle A. J., Owocki S. P., Shaviv N. J., 2008, *MNRAS*, 389, 1353

Vishniac E. T., 1994, *ApJ*, 428, 186

Waxman E., Katz B., 2017, Handbook of Supernovae. Springer International Publishing AG, New York, p. 967

Weiler K. W., Panagia N., Sramek R. A., 1990, *ApJ*, 364, 611

Werner M. W. et al., 2004, *ApJS*, 154, 1

Wilson J. C. et al., 2004, in Moorwood A. F. M., Iye M., eds, SPIE Conf. Ser. Vol. 5492, Ground-based Instrumentation for Astronomy. SPIE, Bellingham, p. 1295

Yaron O. et al., 2017, *Nature Phys.*, 13, 510

This paper has been typeset from a TeX/LaTeX file prepared by the author.